Inhomogeneous alloying in FePt nanoparticles as a reason for reduced magnetic moments



2009 J. Phys.: Condens. Matter 21 336002

(http://iopscience.iop.org/0953-8984/21/33/336002)

J. Phys.: Condens. Matter **21** (2009) 336002 (12pp) doi:10.1088/0953-8984/21/33/336002

# Inhomogeneous alloying in FePt nanoparticles as a reason for reduced magnetic moments

**C Antoniak[1], M Spasova[1], A Trunova[1], K Fauth[2], F Wilhelm[3], A Rogalev[3], J Minár[4], H Ebert[4], M Farle[1] and H Wende[1]**

[1] Fachbereich Physik and Center for Nanointegration Duisburg-Essen (CeNIDE), Universität Duisburg-Essen, Lotharstraße 1, D-47048 Duisburg, Germany
[2] Experimentelle Physik IV, Universität Würzburg, Am Hubland, D-97074 Würzburg, Germany
[3] European Synchrotron Radiation Facility (ESRF), 6 Rue Jules Horowitz, BP 220, F-38043 Grenoble Cedex, France
[4] Department Chemie und Biochemie, Ludwig-Maximilians-Universität München, Butenandtstraße 11, D-81377 München, Germany

E-mail: carolin.antoniak@uni-due.de

Received 6 March 2009, in final form 1 July 2009
Published 24 July 2009
Online at stacks.iop.org/JPhysCM/21/336002

**Abstract**
The reduced magnetic moments of oxide-free FePt nanoparticles are discussed in terms of lattice expansion and local deviation from the averaged composition. By analyses of the extended x-ray absorption fine structure of FePt nanoparticles and bulk material measured both at the Fe K and Pt $L_3$ absorption edge, the composition within the single nanoparticles is found to be inhomogeneous, i.e. Pt is in a Pt-rich environment and, consequently, Fe is in an Fe-rich environment. The standard Fourier transformation-based analysis is complemented by a wavelet transformation method clearly visualizing the difference in the local composition. The dependence of the magnetic properties, i.e. the element-specific magnetic moments on the composition in chemically disordered $Fe_xPt_{1-x}$ alloys, is studied by fully relativistic SPR-KKR band structure calculations supported by experimental results determined from the x-ray magnetic circular dichroism of 50 nm thick films and bulk material.

(Some figures in this article are in colour only in the electronic version)

## 1. Introduction

$Fe_xPt_{1-x}$ nanoparticles are currently the object of intense research activity, driven both by fundamental interest and their possible use as new ultra-high density magnetic storage media (see, e.g., [1–7]). For the latter case, nanoparticles with a high magnetocrystalline anisotropy (MCA) are needed to overcome the superparamagnetic limit, i.e. data loss caused by thermally activated magnetization fluctuations. In addition, the magnetic moments of the nanoparticles should be low to prevent magnetization switching caused by magnetic dipole interactions.

One of the prime candidates for future applications is $Fe_xPt_{1-x}$ in the chemically ordered state around the equi-atomic composition due to its high MCA density [8–11] of about $6 \times 10^6$ J m$^{-3}$. Interestingly, the magnetic moments in FePt nanoparticles in both the chemically disordered and chemically ordered phase are rather small compared to the bulk material [12, 13]. The formation of the chemically ordered $L1_0$ state is driven by volume diffusion and is kinetically suppressed. Annealing of the nanoparticles is suitable to achieve the (partial) $L1_0$ phase in nanoparticles [4, 15–20]. Possibilities to boost Fe and Pt diffusion are, for example, He-ion irradiation [21] or nitrogenization in the case of nanoparticles prepared by gas phase condensation [19].

However, the anisotropy of non-agglomerated nanoparticles with a diameter around 6 nm was found to be almost one order of magnitude smaller than in the bulk material, which

 

may be related to a lower degree of chemical order within the nanoparticles [12, 13].

In order to understand the diffusion processes and possible obstructions towards the $L1_0$ formation, it is necessary to structurally characterize also the chemically disordered nanoparticles in detail as done in this work.

By the analyses of the extended x-ray absorption fine structure (EXAFS) of oxide-free $Fe_{0.56}Pt_{0.44}$ nanoparticles, a lattice expansion was found in our earlier work [22]. The new result of the present paper is clear evidence for an inhomogeneous alloying within the particles. For this purpose, the local composition is determined around Pt and Fe probe atoms, i.e. the EXAFS is analysed at both the Pt $L_3$ and Fe K absorption edges, respectively. Besides the usual Fourier interpretation of the EXAFS, a complementary wavelet transformation (WT) method, adapted from acoustic emission analyses, is employed. It is presented as a method to distinguish between different atomic species in an alloy and a possibility to visualize differences in the local composition around the absorbing atom.

The influence of an inhomogeneous composition within FePt nanoparticles on the magnetic properties, especially on the element-specific magnetic moments, is discussed. As a reference, magnetic moments of chemically disordered $Fe_xPt_{1-x}$ alloys were probed as a function of Fe content by the analysis of the x-ray magnetic circular dichroism (XMCD) of different samples, i.e. bulk material and films of 50 nm thickness. In addition, band structure calculations were performed for $Fe_xPt_{1-x}$ bulk material using the spin-polarized relativistic Korringa–Kohn–Rostoker (SPR-KKR) method.

The organization of this paper is as follows. In section 2, the sample preparation and the x-ray absorption experiments are described. In section 3, a short overview of the input details for the SPR-KKR calculations, XMCD and EXAFS analysis methods is given. The latter were performed using FEFFIT [14] on the one hand and, on the other hand, wavelet transformation was used especially for a better visualization of the results. In section 4, the results of SPR-KKR calculations and x-ray absorption experiments are presented which are discussed in section 5. Finally, in section 6, conclusions are given.

## 2. Experimental details

### 2.1. Sample preparation

Monodisperse single-crystalline $Fe_xPt_{1-x}$ nanoparticles surrounded by oleic acid and oleyl amine were wet-chemically synthesized by the reduction of $Pt(acac)_2$ and thermal decomposition of $Fe(CO)_5$ as described elsewhere [23]. The particles were deposited onto a naturally oxidized Si wafer using the spin coating technique. The particles tend to self-assemble in a short-range hexagonal order [22, 25] and the organic ligands prevent the particles from agglomeration as can be seen in the scanning electron microscopy (SEM) image in figure 1.

Here, two different samples are discussed with different sizes and slightly different compositions. The element-specific magnetic moments were determined for $Fe_xPt_{1-x}$

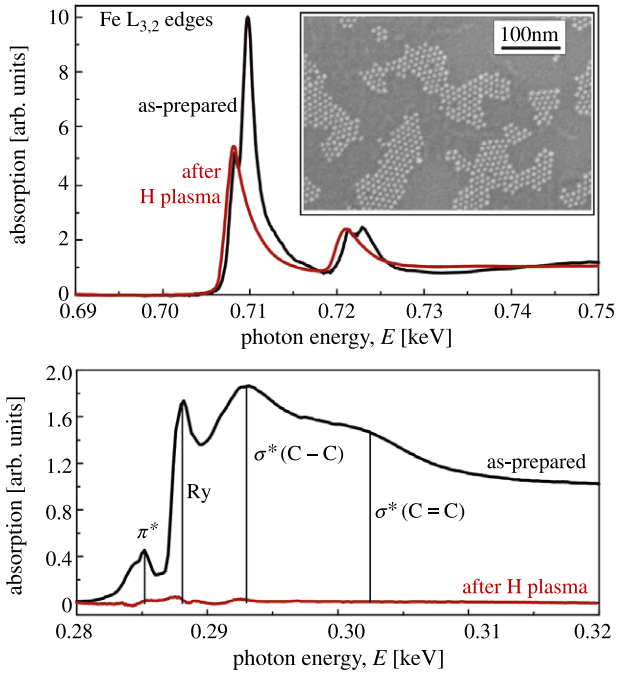


**Figure 1.** XANES at the carbon K and the Fe $L_{3,2}$ absorption edges of FePt nanoparticles on a naturally oxidized Si substrate before (black lines) and after (red lines) hydrogen plasma cleaning [25]. At the carbon K edge, the spectra were normalized to the absorption signal of a clean substrate. The inset shows an SEM image of the sample.

nanoparticles with an Fe content of (50 ± 5) at.% and a mean diameter of 6.3 nm and for particles with an Fe content of (56± 6) at.% and a mean diameter of 4.4 nm. The Fe content was determined by energy-dispersive x-ray spectroscopy (EDS) in a transmission electron microscope.

In order to obtain magnetic moments of pure metallic particles, Fe oxides and organic ligands were removed *in situ* by a soft hydrogen plasma treatment [24]. The plasma is ignited at a hydrogen pressure of about 50 Pa at the standard radio-frequency of 13.56 MHz and a power of 50 W. Afterwards, the pressure was reduced to 5 Pa and the sample was transferred into the plasma chamber where it was exposed to the plasma for 30 min. The efficiency of this treatment was checked by measurements of the XANES at both the Fe $L_{3,2}$ and carbon K absorption edges. It was found that the Fe became completely metallic, i.e. the oxides were reduced, and the absence of any carbon absorption line indicates that the organic ligands were removed completely [25]. This is shown in figure 1: in the as-prepared state, several absorption peaks at the carbon K edge that can be assigned to electron excitation into different molecular states could be obtained. By comparison with spectra of alkanes and alkenes reported in the literature [26, 27], the final states are identified to be $\pi^*$ antibonding states at 285.1 eV, so-called Rydberg states at 288.1 eV (3s, 3d not resolved energetically), $\sigma^*$(C–C) antibonding states of carbon–carbon single bonds at 292.9 eV and $\sigma^*$(C=C) antibonding states of carbon–carbon double bonds around 302 eV. Additional carbon contaminations which are unavoidable even in ultra-high vacuum conditions may contribute to the signal at the carbon K edge. Therefore, the

spectrum was normalized to the absorption of a clean naturally oxidized Si substrate, as was used for the deposition of the particles.

Epitaxial $Fe_xPt_{1-x}$ films with thicknesses around 50 nm were grown on MgO(001) substrates at room temperature by magnetron co-sputtering from Fe and Pt targets in a vacuum system with a base pressure of about $10^{-6}$ Pa. The deposition rate was about 0.1 nm $s^{-1}$. X-ray diffraction (XRD) indicates a high degree of structural order and the mosaic spread is below 1°. The layer thickness determined by Rutherford backscattering was found to be around (46 ± 6) nm and therefore the films are expected to exhibit bulk properties.

A polycrystalline $Fe_{0.56}Pt_{0.44}$ bulk sample was prepared by arc melting in an Ar atmosphere. For all samples, the composition was determined by EDS.

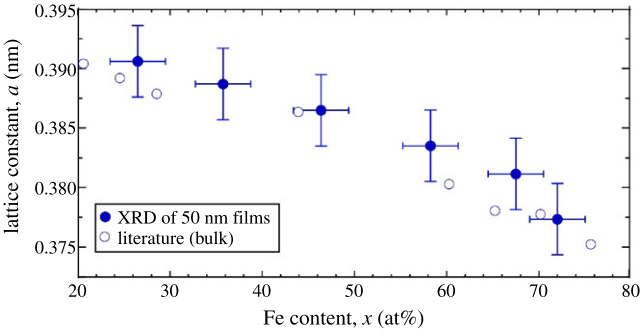


**Figure 2.** Lattice constants determined by XRD of 50 nm thick bulk-like $Fe_xPt_{1-x}$ films as a function of Fe content. Values for $Fe_xPt_{1-x}$ bulk material taken from the literature [30] are shown for comparison.

### 2.2. *X-ray absorption experiments*

The x-ray absorption near-edge structure (XANES) and its associated XMCD was measured in the soft x-ray regime at the Fe $L_{3,2}$ absorption edges at the bending magnet beamline PM3 at BESSY II, Berlin (Germany). The measurements were done at $T = 15$ K in magnetic fields of $\mu_0 H_{\rm ext} = \pm 2.8$ T at fixed photon helicity in an energy range of 0.680 keV $\leqslant E \leqslant$ 0.780 keV. After each scan, the magnetic field was reversed.

Measurements at the Pt $L_{3,2}$ absorption edges in the hard x-ray regime were performed at the ID12 undulator beamline at the ESRF, Grenoble (France) at $T = 7$ K and in magnetic fields up to $\mu_0 H_{\rm ext} = \pm 6$ T. After each scan, either the magnetic field or the helicity of x-ray photons was reversed. XANES and XMCD spectra were taken in the energy range of 11.538 keV $\leqslant E \leqslant$ 11.645 keV and 13.244 keV $\leqslant E \leqslant$ 13.374 keV. The EXAFS at the Pt $L_3$ absorption edge was measured up to 12.581 keV, corresponding to a photoelectron wavenumber $k \approx 140$ $nm^{-1}$, and at the Fe K edge in the range of 7.066 keV $\leqslant E \leqslant$ 8.319 keV.

A portable plasma chamber was attached to the experimental endstations for an *in situ* cleaning of the samples.

## 3. *Ab initio* calculations and data analysis

### 3.1. *SPR-KKR calculations*

The electronic and magnetic properties of chemically disordered $Fe_xPt_{1-x}$ alloys were investigated by means of the fully relativistic spin-polarized version of the KKR band structure method (SPR-KKR) [28] within the framework of spin density functional theory. For the corresponding exchange correlation potential, the local spin density approximation (LSDA) parametrization of Vosko *et al* [29] has been used.

The SPR-KKR method represents the electronic structure in terms of the Green's function evaluated by means of multiple scattering theory. This feature allowed us to deal with the chemical disorder by using the coherent potential approximation (CPA) alloy theory.

The integration in the Brillouin zone was done over a regular $k$-point grid with 225 points. The angular momentum expansion cutoff was set to $l_{\rm max} = 3$. Larger values for the cutoff yield only small changes for the magnetic moments of less than 1%.

As structural input for the SPR-KKR calculations, lattice constants of 50 nm thick single-crystalline $Fe_xPt_{1-x}$ films obtained by x-ray diffraction (XRD) were used which are in agreement with values reported in the literature [30] (figure 2). For the alloys with an Fe content of 27 at.% $\leqslant x \leqslant$ 67 at.%, the lattice constant depends linearly on $x$. For an Fe content of 72 at.% the lattice constant is smaller than expected from linear extrapolation, a first indication of the drop of the lattice constant to (0.3707 ± 0.002) nm at 77 at.% Fe. At this concentration, the crystal structure is already bcc as for bulk Fe.

### 3.2. *Sum-rule-based analysis of XMCD*

To separate the transitions into the 3d states of the Fe atoms and into the 5d final states of the Pt atoms from transitions into higher levels (or into the continuum), a two-step-like function was subtracted in the case of the XANES at the Fe $L_{3,2}$ edges. Since the absorption at the Pt $L_{3,2}$ edges is not well pronounced, this procedure would lead to a large error. Therefore, reference spectra of Au are shifted in energy and subtracted instead [31] after stretching the energy scale to account for the different lattice constants in Au with respect to FePt. As an example, XANES and XMCD spectra of Fe and Pt measured at the $L_{3,2}$ absorption edges of plasma-cleaned FePt nanoparticles with a mean diameter of 6.3 nm are shown in figure 3(a). Note that the XMCD in the case of Pt is enlarged by a factor of 4. In addition, the two-step-like function and the modified Au reference spectra are shown. Subtracting these spectra from the experimental XANES leads to the XANES corresponding to electron excitation into 3d (5d) final states for Fe (Pt) shown in figures 3(b) and (c). The effective spin magnetic moment $\mu_S^{\rm eff}/n_h$ and the orbital magnetic moment $\mu_l/n_h$ per unoccupied final state $n_h$ can be determined according to the sum rules [33, 34] that can be written as [32]

$$\frac{\mu_l}{n_h} = -\frac{2}{3}\frac{q}{r}\,\mu_{\rm B} \tag{1}$$

$$\frac{\mu_s^{\rm eff}}{n_h} = \frac{-3p+2q}{r}\,\mu_{\rm B}, \tag{2}$$

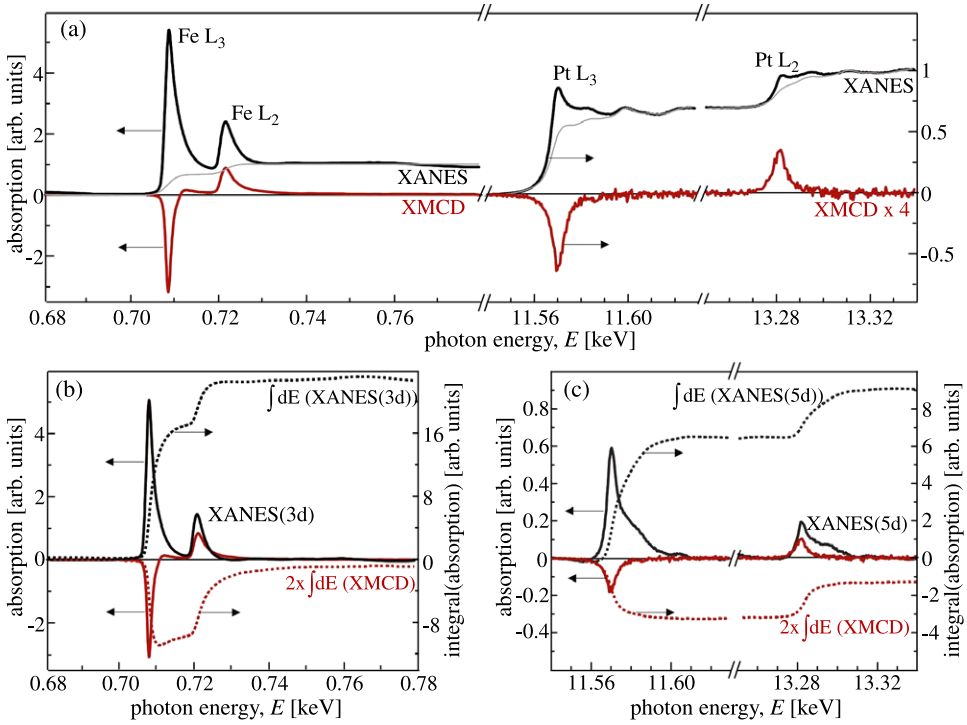


**Figure 3.** (a) XANES (black lines) and its associated XMCD (red lines) at both Fe and Pt $L_{3,2}$ absorption edges of 6.3 nm FePt nanoparticles. Note the different scaling of the ordinate for Fe and Pt absorption spectra. In addition, the XMCD signal at the Pt edges is enlarged by a factor of 4. Light grey lines refer to a two-step-like function in the case of Fe and modified Au reference spectra in the case of Pt. (b), (c) XANES, XMCD and their integrals (dashed lines) after background (light grey lines in (a)) subtraction. The integral of XMCD is enlarged by a factor of 2 for both Fe and Pt.

where $p$ is the integral of XMCD over the energy range of $L_3$ absorption edge, $q$ is the integral of XMCD over the energy range of $L_3$ and $L_2$ absorption edges, and $r$ is the integral of XANES(3d) in the case of Fe and XANES(5d) in the case of Pt over the energy range of $L_3$ and $L_2$ absorption edges. The quality of the integrals of experimental data presented in figure 3 is sufficient to extract the values for $p$, $q$ and $r$ validating the procedure of background subtraction using Au reference spectra in the case of Pt.

For the numbers of unoccupied final states $n_h(\mathrm{Fe}) \approx 3.41$ at the Fe sites and $n_h(\mathrm{Pt}) \approx 1.74$ at the Pt sites were used as obtained from band structure calculations. Due to the procedure of background subtraction, the spectra in figure 3(c) correspond to a number of unoccupied final 5d states $\tilde{n}_h(\mathrm{Pt}) = n_h(\mathrm{Pt}) - n_h(\mathrm{Au})$ with $n_h(\mathrm{Au}) = 0.75$.

Note that the effective spin magnetic moment $\mu_S^{\mathrm{eff}} = \mu_S + 7\mu_t$ consists of the spin magnetic moment and a magnetic dipole moment accounting for a possible asphericity of the spin density distribution.

Measurements performed in the total electron yield (TEY) mode were corrected for saturation effects [35, 36] using an electron escape depth of 2 nm. Variation of the escape depth between 1.7 and 2.5 nm did not have any visible effect on the saturation. For a reliable correction of saturation effects it is further necessary to obtain the absorption coefficient in absolute values from the measured TEY in arbitrary units. Therefore the spectra were fitted in the pre- and post-edge regions to the calculated absorption coefficient of non-resonant absorption [37]. Measurements of the TEY signal at different angles between the incident x-rays and the sample normal improved the accuracy.

### 3.3. EXAFS analysis and simulations

The EXAFS oscillations $\chi(k)$ were extracted from experimental absorption data by fitting and subtracting the atomic background using the AUTOBK algorithm [38] with a threshold frequency $R_{\mathrm{bkg}} = 0.11$ nm. For Fourier transformation of the experimental data as a function of photoelectron wavenumber $k$, the $k$ weighted data were used in the range between $k_{\mathrm{min}} \approx 20\ \mathrm{nm}^{-1}$ and $k_{\mathrm{max}} \approx 125\ \mathrm{nm}^{-1}$ in a Kaiser–Bessel window with $\mathrm{d}k = 1\ \mathrm{nm}^{-1}$. For Fourier transformation of the experimental data obtained at the Fe K edge of the nanoparticles, a smaller $k$ range between $k_{\mathrm{min}} \approx 20.0\ \mathrm{nm}^{-1}$ and $k_{\mathrm{max}} \approx 80\ \mathrm{nm}^{-1}$ had to be used since the data are more noisy (figure 6).

For the calculation of the scattering paths $j$, and the simulation of the EXAFS respectively, the structure of the material has to be put in, i.e. the position and the type of element of the absorber and backscatterer. The calculation of the scattering paths was done using the software *Artemis* [39] based on the algorithms of the FEFFIT [14] and FEFF [40, 41] programs.

In these programs, the full $\chi(k)$ spectrum is represented as the sum of the imaginary part of contributions from different paths:

$$\chi(k) = \sum_j \mathrm{Im}\,(\tilde{\chi}_j(k)) \qquad (3)$$

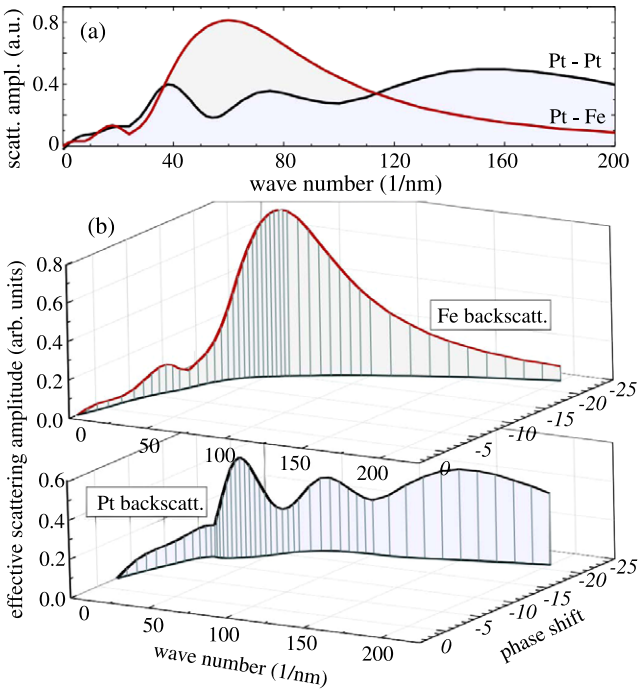


**Figure 4.** (a) Backscattering amplitude of Fe and Pt as a function of photoelectron wavenumber. (b) Effective backscattering amplitude of Fe and Pt and EXAFS phase shift as a function of the photoelectron wavenumber. The grey line in the coordinates plane at the bottom refer to the dependence of the phase shift on the wavenumber. In all cases Pt is the absorber atom.

where $\tilde{\chi}_j(k)$ is the contribution calculated from a particular scattering path $j$ that may either be a single or a multiple scattering path and can be written as

$$\tilde{\chi}_j(k) = \frac{S_0^2 N_j^* F_j(k)}{kR_j^2} \exp[2ikR_j + i\delta_j(k)] \times \exp[-2R_j/\lambda(k) - 2k^2\sigma_j^2]. \quad (4)$$

In this equation, $S_0^2$ denotes an amplitude reduction factor due to many-body effects, $N_j^*$ is the effective coordination number, $F_j(k)$ is the effective scattering amplitude, $R_j$ is half the total length of the scattering path, $\lambda(k)$ is the mean free path length of the photoelectron with wavenumber $k$, $\delta_j$ is an effective total phase shift (including contributions from the central atom and all scattering atoms) and $\exp[-2\sigma_j^2k^2]$ is the EXAFS Debye–Waller factor. In figure 4, the EXAFS phase shifts and effective backscattering amplitudes for Fe and Pt are shown as a function of wavenumber. The correspondence of the variables in equation (4) to the entries of an FEFF output file is [43]

$$\text{mag[feff]} \times \text{red factor} \longrightarrow F_j(k)$$

$$\text{real}[2 * \text{phc}] + \text{phase[feff]} \longrightarrow \delta_j(k)$$

where 'mag[feff]' denotes the backscattering curved wave amplitude and 'red factor' is a reduction factor that approximates the losses due to multiple electron excitations at the absorbing atom caused by the creation of a core hole in x-ray absorption experiments. 'real[2*phc]' is twice the real part of the central atom phase shift and 'phase[feff]' is the backscattering curved wave phase. More detailed information about the notation in FEFF codes, input and output files can be found elsewhere [42, 43].

The backscattering amplitude is also shown as a 2D graphic in figure 4(a) for an easier reading of the $k$ values of interesting points of the backscattering amplitude, e.g. maxima and minima. Fe has the maximum backscattering amplitude at $k \approx 60$ nm$^{-1}$. At this $k$ value the backscattering amplitude of Pt atoms exhibits a local minimum. The strong reduction in the Pt amplitude over a small range at this point is connected with a more rapidly changing phase. This effect is known in the literature as the generalized Ramsauer–Townsend effect [44, 45]. In a simple picture, the wavelength of the outgoing photoelectron (about 0.1 nm for $k \approx 60$ nm$^{-1}$) is well matched to the size of the scatterer. In this case, the photoelectron may tunnel through the scattering potential and the scattering cross section vanishes, leading to a dip in the backscattering amplitude at a fairly distinct wavenumber.

In order to fit the calculated EXAFS signal to the experimentally obtained one, FEFFIT uses the cumulant expansion [46, 47] with the first four cumulants ($\Delta R$, $\sigma^2$, $C_3$, $C_4$) of the pair distribution function of atoms around the absorber atom. Accounting for thermal or configurational disorder, the complex wavenumber $p$ is introduced and should be used instead of $k$. The imaginary part of $p$ represents losses of photoelectron coherence including the mean free path and core-hole lifetime. The resulting modified EXAFS equation can be written as [42]

$$\tilde{\chi}_j = \frac{S_0^2 N_j^* F_j(k)}{k(\Delta R_j + R_j)^2} \exp[2ikR_j + i\delta_j(k)] \times \exp[2i(p\Delta R_j - 2p\sigma_j^2/R_j - 2p^3 C_{3,j}/3)] \times \exp[-2R_j/\lambda(k) - 2p^2\sigma_j^2 - 2p^4 C_{4,j}/3]. \quad (5)$$

It turned out that, for the data examined here, it is not necessary to include the fourth-order cumulant in the fitting procedure. Even the third cumulant accounting for an anharmonicity of the interatomic potential does not have to be included for a proper simulation of the experimental data presented here.

To model the chemically disordered $Fe_xPt_{1-x}$ alloys, fitting of the experimental data was performed using the sum of EXAFS calculated for the absorber in a pure fcc Fe environment and in a pure fcc Pt environment, respectively, with the same distance of nearest neighbours. The overall amplitudes for these two cases is a measure of the Fe and Pt content.

Especially in alloys, it is interesting to distinguish between the contributions of the different atomic species located at the same distance to the EXAFS signal. A powerful tool to visualize these contributions is the use of wavelet transformation (WT) [48]. Like the Fourier transformation, the WT is a mathematical complete transformation, i.e. the backward WT recovers the original data again [49]. The main idea behind WT is to replace the infinitely expanded periodic oscillations in a Fourier transformation by located wavelets as a kernel for the integral transformation.

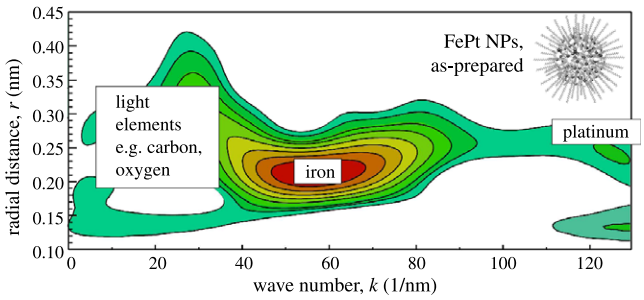


**Figure 5.** Contour plot of the wavelet-transformed EXAFS of $Fe_xPt_{1-x}$ nanoparticles in the as-prepared state.

One may realize the WT as an improved short-term Fourier transformation (STFT) which determines the Fourier coefficients of the original data multiplied by a window function, i.e. the $k$-dependent EXAFS data are transformed in several intervals of $k$. In STFT, a high resolution in $k$ yields a low resolution in $r$ and vice versa. By contrast, the advantage of WT is the use of a *scalable* mother wavelet or analysing wavelet $\psi(k)$ as a window function for the transformation. The basis of the transformed signal is generated not only by translation, but also by scaling of the analysing wavelet yielding high resolution both in $k$ and $r$ space. In this work, the AGU-Vallen wavelet software was used [50], which was developed for acoustic emission analyses, but can easily be adapted for EXAFS analyses. As analysing wavelet, a Gabor wavelet based on the Gaussian function is used. It has the form

$$\psi(k) \propto \left(\frac{r_c}{\gamma}\right)^{1/2} \exp\left[-\frac{1}{2}\left(\frac{r_c k}{\gamma}\right)^2 + \mathrm{i} r_c k\right] \qquad (6)$$

with a centre length $r_c$ and a constant $\gamma$ which determines resolutions both of the dimensioning in $k$ and of the bandwidth in $r$. This parameter is chosen to be $\gamma = \pi\sqrt{2\ln 2}$ to satisfy the admissibility condition, i.e. the integral over a wavelet is zero and the wavelet functions satisfy the orthonormality condition [50].

In EXAFS analysis, the $k$ dependence of the absorption signal can be resolved by WT. Figure 5 shows the WT of $Fe_xPt_{1-x}$ nanoparticles in the as-prepared state containing also Fe oxides and organic ligands at the surface. It was chosen as one example of a sample that consists not only of a binary alloy but also of light elements like carbon and oxygen. The $k$ position of maxima in the WT is connected to the different elements via the individual $k$ positions of their maximum backscattering amplitude. Thus, the WT maxima at low $k$ values correspond to the EXAFS signal of light elements like carbon and oxygen. It can even be distinguished between the contribution of the Fe and Pt atoms in the $Fe_xPt_{1-x}$ alloy with the same nearest-neighbour distance, since the $k$ value of the maximum of the WT differs significantly for the lighter ($Z_{Fe} = 26$) and the heavier ($Z_{Pt} = 78$) backscattering atoms. Note that there is a shift between the radial distance $r$ in the plot and the geometrical distance between nearest-neighbour atoms due to the EXAFS phase shift.

## 4. Results

### *4.1. Crystal structure and alloying in FePt nanoparticles*

XRD, electron diffraction (ED) and high-resolution transmission electron microscopy (HR TEM) [51] analyses indicate a lattice expansion in $Fe_xPt_{1-x}$ nanoparticles in comparison to the corresponding bulk material. By the analysis of the EXAFS oscillations of hydrogen-plasma-cleaned nanoparticles, it has already been shown that this lattice expansion is an intrinsic property of the nanoparticles and is neither caused by the organic ligands surrounding the nanoparticles nor by Fe oxides that are present in as-prepared nanoparticles exposed to air [22].

Here, we focus on the local composition determined by EXAFS. The $k$-weighted experimental data and the result of the simulations that fit best are shown in figure 6. The window used for Fourier transformation of the data is also outlined. Note that the maximum value of the window function equals 1. The Fourier transform of the experimental EXAFS data of both $Fe_{0.56}Pt_{0.44}$ bulk material and plasma-cleaned nanoparticles and the simulations that fit best are shown as a function of radial distance. Fitting of the calculated Fourier transform was performed in the range between $r \approx 0.11$ and 0.34 nm; only nearest-neighbour contributions are included.

Before turning to the case of the nanoparticle system, EXAFS results of the bulk reference sample will be compared to the lattice constant and composition determined by other methods. The best fit to the experimental EXAFS data was obtained for simulations assuming $(59 \pm 4)$ at.% Fe around the Pt probe atoms and $(55 \pm 6)$ at.% around the Fe probe atoms. These values are the same within experimental errors and are in good agreement with the Fe content determined by EDS ($(56 \pm 3)$ at.%). Additionally, the lattice constant used in the simulations, i.e. 0.383 nm, equals the lattice constant obtained from XRD $(0.384 \pm 0.002)$ nm. The error of lattice constants determined by EXAFS analysis was estimated by varying the lattice constant in the simulations.

In the case of nanoparticles, the reduction of the envelope of EXAFS oscillations due to the Ramsauer–Townsend effect in Pt corresponds to a reduction of the amplitude of the Fourier transform in a small region of $r$ around $r \approx 0.21$ nm. This reduction is strongly pronounced in the case of the EXAFS data measured at the Pt $L_3$ absorption edge of the nanoparticles, indicating a Pt enrichment around the Pt probe atoms. In fact, in the nanoparticles $(40 \pm 8)$ at.% Fe has to be assumed for a proper simulation of the experimental data measured at the Pt $L_3$ edge which does not match the value found by EDS ($(56 \pm 5)$ at.% Fe). This difference is not a conflict between EXAFS and EDS results, but simply reflects that an averaging technique like EDS does not allow for the detection of an inhomogeneous composition of the investigated sample whereas the EXAFS technique does. The reason is that EXAFS stems from scattering of the photoelectron at the local surrounding of the probe atoms. Thus, it can be concluded that the Pt absorbing atoms are in a Pt-rich environment and the Fe atoms are in an Fe-rich environment. From the Fe content around the Pt atoms and the averaged value, the Fe content in the near environment of the Fe atoms is expected to

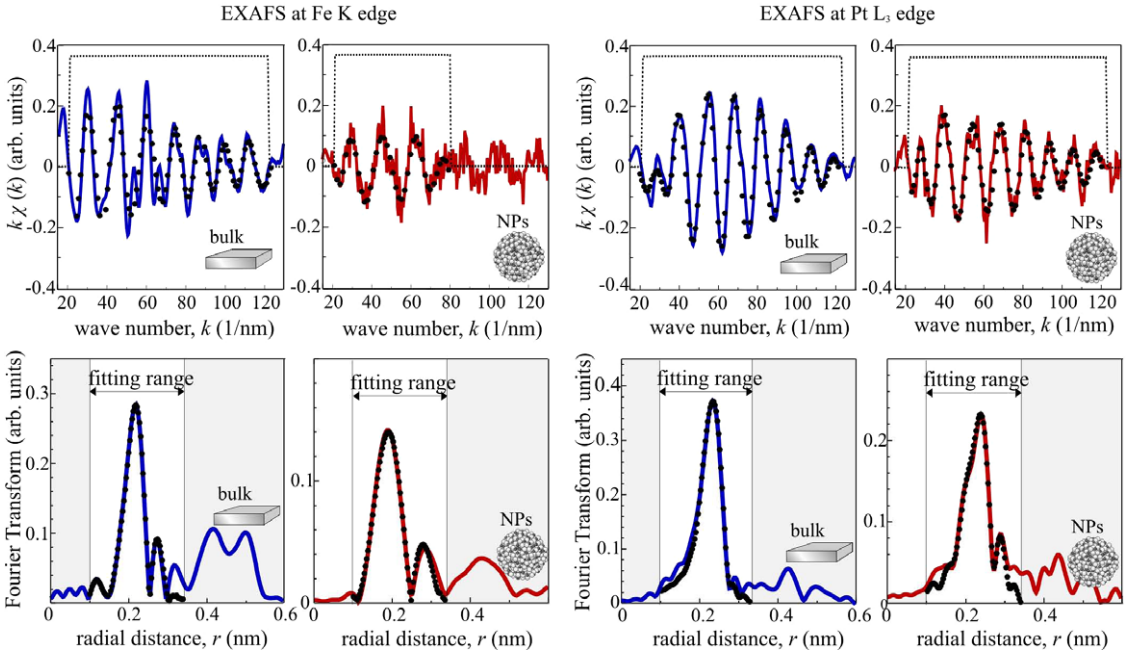


**Figure 6.** Upper graphics: EXAFS data measured at room temperature at the Fe K absorption edge (left panel) and Pt $L_3$ absorption edge (right panel) and simulations (filled circles) of bulk $Fe_{0.56}Pt_{0.44}$ (blue solid lines) and $Fe_{0.56}Pt_{0.44}$ nanoparticles (red solid lines). The dashed line corresponds to the window used for Fourier transformation. Lower graphics: Fourier transform of experimental EXAFS data (lines) shown in the upper graphics and simulations (filled circles). A smaller window for the Fourier transformation had to be used for the data measured at the Fe K edge of nanoparticles causing a slightly different shape and position of centroid.

**Table 1.** Lattice constant at room temperature of $Fe_{0.56}Pt_{0.44}$ nanoparticles and the corresponding bulk alloy determined by different methods (cf [22]).

| | Lattice constant, $a$ (nm) | |
|---|---|---|
| Method | Bulk material | Nanoparticles |
| Fe EXAFS | $0.383 \pm 0.004$ | $0.387 \pm 0.008$ |
| Pt EXAFS | $0.383 \pm 0.003$ | $0.387 \pm 0.004$ |
| XRD | $0.384 \pm 0.002$ | $0.388 \pm 0.002$ |
| HR TEM, ED | — | $0.389 \pm 0.006$ |

**Table 2.** Composition of $Fe_{0.56}Pt_{0.44}$ nanoparticles and the corresponding bulk alloy determined by different methods. The composition obtained by EXAFS is given by the local composition (first shell) around the Fe probe atoms and the Pt probe atoms, respectively.

| | Fe content, $x$ (at.%) | |
|---|---|---|
| Method | Bulk material | Nanoparticles |
| Fe EXAFS | $55 \pm 6$ | $70 \pm 12$ |
| Pt EXAFS | $59 \pm 4$ | $40 \pm 8$ |
| EDS | $56 \pm 3$ | $56 \pm 6$ |

be around 72 at.%. The analysis of the experimental EXAFS data measured at the Fe K edge support this conclusion, i.e. the Fe probe atoms are in an Fe-rich environment containing $(70 \pm 12)$ at.% Fe. Note that the larger error bar is due to the smaller $k$ range of Fourier transformation accounting for the smaller signal-to-noise ratio in the EXAFS spectrum (figure 6). In tables 1 and 2, the lattice constants and Fe contents are summarized.

Within experimental errors, no different lattice constants for the Fe-rich and Pt-rich regions were found in the nanoparticles. One may argue that the differences in the EXAFS of the nanoparticles compared to the bulk EXAFS is an effect of a flat and asymmetric pair potential at the surface caused by a reduced coordination number. But, in fact, introducing a non-vanishing third cumulant which describes such an effect yields a stretching of the EXAFS at higher $k$ values (contraction of the nearest-neighbour distance) which was not observed here. Even with a small but reasonable value of $c_3 = 10^{-7}$ nm$^3$ it is not possible to simulate the experimental data properly.

To visualize the different Fe and Pt contents around the probe atoms in the bulk material and in the nanoparticles, the WT method was employed. Since the effects are rather small, in figure 7 the difference of the bulk and nanoparticle EXAFS is shown, i.e. the wavelet transformed bulk data were subtracted from the wavelet-transformed nanoparticle data. The analysed data measured at the Pt $L_3$ edge show a clear minimum at $k \approx 60$ nm$^{-1}$, $r \approx 0.21$ nm (figure 7 (right)), indicating less Fe nearest-neighbour atoms of the Pt probe atoms than in the bulk alloy. Accordingly, at approximately the same radial distance the WT is increasing at high $k$ values, indicating a higher probability to find Pt atoms as nearest neighbours of the Pt absorbing atoms. The slightly different $r$ values of Fe and Pt maxima may be due to different backscattering phases [48]. Although the experimental data obtained at the Fe K edge are noisy for higher values of $k$, the results using WT are reasonable. A maximum at low $k$ values and a (less pronounced) minimum at high $k$ values shown in figure 4 (left) indicate more Fe and less Pt atoms around

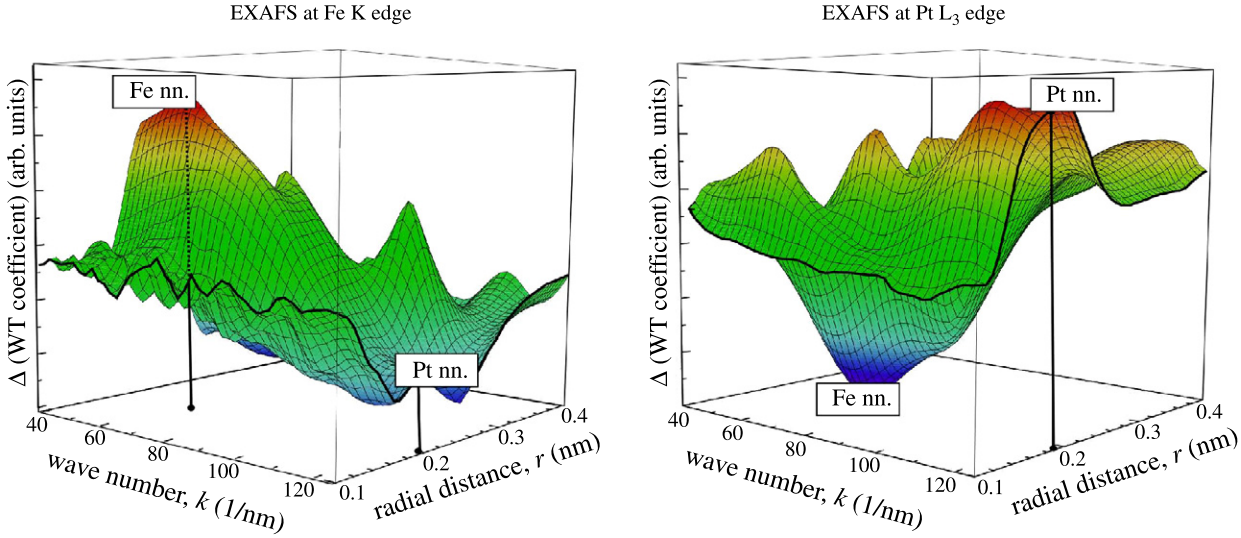


**Figure 7.** 3D surface plot of the difference between wavelet-transformed EXAFS of Fe and Pt absorber atoms in nanoparticles and bulk material. The difference measured at the Fe K edge (left) reveals the change around the Fe sites whereas the difference measured at the Pt $L_3$ absorption edge (right) reveals the change in the surrounding of Pt sites. The positions of the Fe and Pt nearest-neighbour (nn) atom backscattering maxima are marked.

the Fe probe atoms in nanoparticles with respect to the bulk material.

### *4.2. Element-specific magnetic moments in $Fe_xPt_{1-x}$ alloys: bulk materials and nanoparticles*

The deviation of the local composition from the averaged value presented in the previous section may strongly influence the magnetic properties of the $Fe_xPt_{1-x}$ nanoparticles, e.g. the element-specific magnetic moments at the Fe and Pt sites as reported in the literature [12, 13, 25]. In order to rate these values experimentally found in nanoparticles (table 3), the corresponding magnetic moments of the bulk materials are needed. In this work, we present not only experimentally obtained magnetic moments of bulk-like $Fe_xPt_{1-x}$ films, but also results of SPR-KKR band structure calculations.

The calculated spin and orbital magnetic moments at both the Fe and Pt sites are given in table 4. We found that the magnetic moment at the Fe sites is increasing with increasing Pt content, whereas the Pt magnetic moments remain largely unchanged. The increase in the case of Fe can be essentially explained by the increase of the lattice constant which usually yields larger magnetic moments in ferromagnetic and antiferromagnetic materials, e.g. in Fe [55]. Due to a reduction in the hybridization of Fe d states, the increase of the magnetic moment at the Fe sites is connected to a sharpening of the density of states (DOS). The calculated DOS is shown in figure 8 for three different compositions, i.e. $Fe_{0.32}Pt_{0.68}$, $Fe_{0.58}Pt_{0.42}$ and $Fe_{0.68}Pt_{0.32}$. Besides the spin-resolved total DOS, the angular momentum (s, p, d)-resolved partial densities of states are also shown. The shape of the DOS is in agreement with the calculated DOS for randomly disordered $Fe_{0.50}Pt_{0.50}$ alloys reported in the literature [52]. In general, the chemical disorder yields rather smooth changes in the DOS, i.e. possible fine structures that may be present for perfectly ordered systems are washed out. At the Fe sites, the relatively narrow d bands are strongly exchange-split. A clear broadening of the DOS at the Fe sites for the Fe-rich alloy is visible and the difference between the majority and the minority band becomes smaller. At the Pt sites, the d bands are broader by a factor of about two and only a slight composition dependence is visible corresponding to an almost constant magnetic moment.

**Table 3.** Experimentally obtained effective spin and orbital magnetic moments at the Fe and Pt sites of $Fe_{0.56}Pt_{0.44}$ bulk material, $Fe_{0.50}Pt_{0.50}$ nanoparticles with a mean diameter of 6.3 nm, and the moments at the Fe sites of $Fe_{0.56}Pt_{0.44}$ nanoparticles with a mean diameter of 4.4 nm. The values taken from [12] were recalculated using $n_h = 3.41$.

| | |
|---|---|
| $Fe_{0.56}Pt_{0.44}$ bulk material | |
| $\mu_S^{\text{eff}}(\text{Fe})/\mu_B$ | $2.59 \pm 0.26$ |
| $\mu_l(\text{Fe})/\mu_B$ | $0.076 \pm 0.014$ |
| $\mu_S^{\text{eff}}(\text{Pt})/\mu_B$ | $0.47 \pm 0.02$ |
| $\mu_l(\text{Pt})/\mu_B$ | $0.045 \pm 0.006$ |
| $Fe_{0.50}Pt_{0.50}$ nanoparticles [12], $d = 6.3$ nm | |
| $\mu_S^{\text{eff}}(\text{Fe})/\mu_B$ | $2.28 \pm 0.25$ |
| $\mu_l(\text{Fe})/\mu_B$ | $0.048 \pm 0.010$ |
| $\mu_S^{\text{eff}}(\text{Pt})/\mu_B$ | $0.41 \pm 0.02$ |
| $\mu_l(\text{Pt})/\mu_B$ | $0.054 \pm 0.006$ |
| $Fe_{0.56}Pt_{0.44}$ nanoparticles, $d = 4.4$ nm | |
| $\mu_S^{\text{eff}}(\text{Fe})/\mu_B$ | $2.13 \pm 0.21$ |
| $\mu_l(\text{Fe})/\mu_B$ | $0.062 \pm 0.014$ |

The averaged total magnetic moment per atom is in perfect agreement with experimental data reported in the literature [54]. In order to compare not only the averaged magnetic moments, but the element-specific spin and orbital magnetic moments, XMCD measurements on a bulk-like system were performed and analysed. The experimental results on 50 nm thick $Fe_xPt_{1-x}$ films are in qualitative agreement

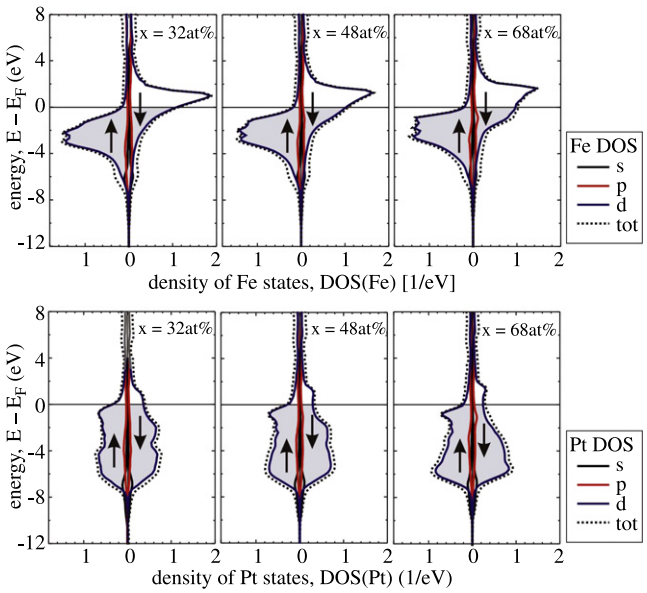


**Figure 8.** Spin-and angular momentum-resolved density of states at the Fe sites (upper panel) and Pt sites (lower panel) calculated for $Fe_xPt_{1-x}$ chemically disordered bulk alloys using $x = 32$ at.%, $x = 48$ at.% and $x = 68$ at.%, respectively.

**Table 4.** Spin and orbital magnetic moments at the Fe and Pt sites in chemically disordered $Fe_xPt_{1-x}$ alloys obtained from SPR-KKR band structure calculations.

| $x$/at.% | 32 | 40 | 48 | 60 | 68 | 72 |
|---|---|---|---|---|---|---|
| $\mu_S$(Fe)/$\mu_B$ | 3.045 | 2.979 | 2.912 | 2.818 | 2.757 | 2.700 |
| $\mu_l$(Fe)/$\mu_B$ | 0.065 | 0.069 | 0.073 | 0.077 | 0.079 | 0.077 |
| $\mu_S$(Pt)/$\mu_B$ | 0.221 | 0.231 | 0.232 | 0.227 | 0.224 | 0.228 |
| $\mu_l$(Pt)/$\mu_B$ | 0.042 | 0.045 | 0.047 | 0.048 | 0.049 | 0.047 |

with the theoretically calculated results, i.e. the spin magnetic moments at the Fe sites are reduced in Fe-rich $Fe_xPt_{1-x}$ alloys (figure 9 in section 5). For Fe contents up to about 50 at.% the calculated values also match quantitatively the experimental data. At the highest Fe content studied in this work (≈70 at.%), the calculated value is larger by about 0.5 $\mu_B$ with respect to the experimentally obtained one. At the Pt sites, the calculated values are smaller by a factor of about two, but in agreement with other calculated values reported in the literature [52]. The reason for this disagreement between theory and experiment is yet unclear.

In the nanoparticles, the effective spin magnetic moment at the Fe sites is reduced by 20–30% with respect to the corresponding bulk material [12, 13] and shows a slight size dependence [25]. The experimentally obtained values are listed in table 3. Note that the values taken from [12] are recalculated for a different number of unoccupied final states that was obtained from SPR-KKR calculations for bulk material as presented in this work, i.e. $n_h = 3.41$ instead of $n_h = 3.705$ which was taken from earlier work [53].

## 5. Discussion

The magnetic moments at the Fe sites of chemically disordered $Fe_xPt_{1-x}$ nanoparticles were found to be reduced by 20–30%

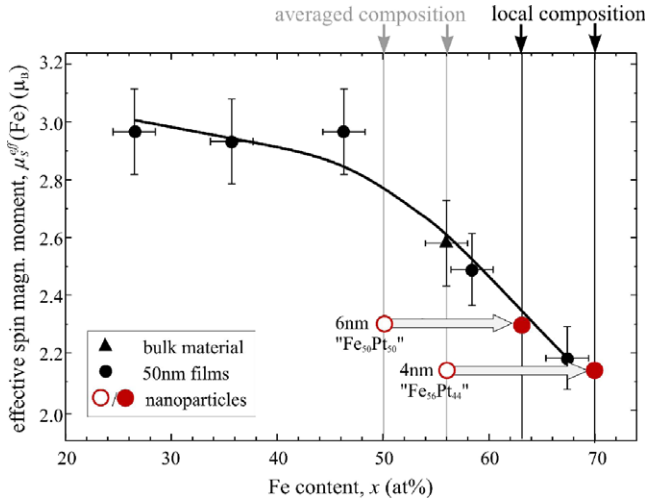


**Figure 9.** Experimentally obtained effective spin magnetic moments at the Fe sites of chemically disordered $Fe_xPt_{1-x}$ films and bulk material, respectively, as a function of Fe content. The moments in nanoparticles are assigned to the averaged compositions determined by EDS. The local composition determined by EXAFS for the 4.4 nm nanoparticles is also marked by an arrow on the top axis. For the 6.3 nm nanoparticles the local composition is estimated assuming the same relative deviation from the averaged value. The light grey arrow in the graph illustrates the difference in averaged and local composition. See tables 2 and 3 for missing error bars.

with respect to the corresponding bulk material [12, 13]. As a consequence, the induced magnetic moments at the Pt sites are also smaller in the nanoparticles. Since the latter are rather small, we focus on the discussion of the magnetic moments at the Fe sites showing significant changes.

There are two possible reasons for the reduced magnetic moments found by EXAFS analysis: the lattice expansion and the inhomogeneous composition. The lattice expansion cannot be the reason for the reduced magnetic moments since a larger lattice constant yields larger magnetic moments at the Fe sites. We validated this by SPR-KKR calculations, which yield a slight increase by 0.6% for the spin magnetic moment at the Fe sites for a lattice constant that is 1% larger than in the bulk (not shown here). Similar trends are reported for other ferromagnetic or antiferromagnetic materials, e.g. for bcc and fcc Fe [55].

However, the deviation of the local composition from the averaged value is an apposite explanation. As presented in this work, the Pt atoms are in a Pt-rich environment compared to the averaged composition, whereas Fe atoms are in an Fe-rich environment in the nanoparticles. In figure 9, the effective spin magnetic moments at the Fe sites of $Fe_xPt_{1-x}$ chemically disordered bulk-like alloys are shown as a function of Fe content. It is clearly visible that $\mu_S^{eff}$ is decreasing monotonically with increasing Fe content. The values of $\mu_S^{eff}$ for $Fe_xPt_{1-x}$ particles are also shown in this graphic. (For more clarity, the errors were omitted in the graph.) The moments are assigned to the averaged compositions of the $Fe_{0.50}Pt_{0.50}$ particles with a mean diameter of 6.3 nm and the $Fe_{0.56}Pt_{0.44}$ particles with a mean diameter of 4.4 nm, respectively. Also the local composition determined from EXAFS analysis is

marked by an arrow at the top axis. Assigning the value of $\mu_S^{eff}$ to this local composition, the nanoparticle data fits within experimental error bars to the moments at the Fe sites in 50 nm thick films.

For the larger particles, no EXAFS data were measured. Therefore, the local composition was estimated assuming the same relative deviation from the averaged value, i.e. an Fe enrichment of about 27% around the Fe atoms. Starting from the averaged composition of $Fe_{0.50}Pt_{0.50}$, this leads to an Fe content of about 63 at.%. Again, assigning the value of $\mu_S^{eff}$ to this local composition, the nanoparticle data fits to the reference curve of the moments of the 50 nm thick films.

This indicates that the inhomogeneous composition within the nanoparticles is very likely the reason for the strongly reduced magnetic moments in the nanoparticles compared to the corresponding bulk material of the same averaged composition.

Note that, from the analyses presented here, it is not possible to specify the inhomogeneity of the alloy, i.e. to distinguish a possible core/shell-like structure from random clustering of the chemical elements within the nanoparticles.

In the literature, several other reasons for reduced magnetic moments in nanoparticles are discussed, e.g. spin canting effects [24] or the influence of an intra-atomic dipole term in the XMCD, the latter being a quite frequent problem of sum-rule-based analysis of XMCD [33, 34] yielding an *effective* spin magnetic moment $\mu_S^{eff}$ per unoccupied final state $n_h$ (cf section 3.2). Although these effects are expected to be too small to cause the distinct drop by 20–30% of the magnetic moment when reducing the system dimension from the bulk to nanoparticles, they will be briefly discussed below for the sake of completeness.

For single-crystalline materials with weak spin–orbit coupling, the magnetic dipole moment $\mu_t$ that contributes to $\mu_S^{eff}$ can be eliminated by angular-dependent measurements of the XMCD [56]. In ensembles of $Fe_xPt_{1-x}$ nanoparticles with a strong spin–orbit coupling, $\mu_t$ cannot be eliminated, and even for randomly oriented crystallographic axes $\mu_t$ will not cancel out [57]. A negative contribution of $\mu_t$ especially from surface atoms reduces $\mu_S^{eff}$ derived from XMCD analysis and will lead to a further decrease for analysed data from nanoparticle systems due to their larger fraction of surface atoms compared to 50 nm thick films or bulk material. One may note that, in the case of Fe nanoclusters, a decrease of $\mu_S^{eff}$ with decreasing size was associated with a negative contribution of $\mu_t$ [58]. This may also be the reason for the slight size dependence found in FePt nanoparticles reported earlier [25].

In addition, changes in the number of unoccupied final states $n_h$ influence the experimentally determined $\mu_S^{eff}$ since this number has to be known for its quantification. For both nanoparticles and films, the same number of $n_h$ was used.

However, these effects mentioned above are too small to cause a reduction of the magnetic moment by 20–30% compared to bulk material. A spin canting effect in nanoparticles can also reduce the measured magnetic moments. It occurs in systems with a high MCA compared to the exchange coupling which favours a collinear alignment of the spins. A magnetic moment that is reduced by 20–30%, as is the case here, corresponds to one or two 'magnetically dead' surface layers, i.e. extremely strong spin canting yielding a vanishing net magnetization that was not obtained in metallic nanoparticles. Such a strong spin canting would also be expected to influence the field-dependent magnetization in a way that at high external magnetic fields a slope should be visible arising from the canted spins that can hardly be forced into the direction of the external field. In magnetic hysteresis on FePt nanoparticle systems measured element-specifically at the Fe $L_3$ edge as presented, for example, in [12, 25] such a slope in the high-field region was not observed, indicating the absence of strongly canted surface spins. From a theoretical point of view, there is the possibility that for nanoparticles a small spin canting may exist [59, 60] if one assumes MCA densities in the volume and at the surface that are even larger than in the chemically ordered FePt $L1_0$ phase [59]. In the low-anisotropic chemically disordered state of FePt investigated in this work, such canting effects are also assumed to be quite unlikely.

In summary, the inhomogeneous composition within the nanoparticles seems to be the most probable explanation for the reduced magnetic moments. Since this reduction is also reported for $Fe_xPt_{1-x}$ nanoparticles around the equi-atomic composition prepared by gas phase condensation, one may conclude that the inhomogeneity can be found in $Fe_xPt_{1-x}$ particles independently of the preparation method. The preferential formation of Fe-rich and Pt-rich regions within the nanoparticles could also influence the formation of the $L1_0$ state and lower the degree of chemical order.

Besides the $Fe_xPt_{1-x}$ system, a local deviation of the composition with respect to the averaged value may also occur in nanoparticles of various binary alloys.

## 6. Conclusion

By the analyses of the EXAFS of hydrogen-plasma-cleaned $Fe_{0.56}Pt_{0.44}$ nanoparticles and bulk material, not only a lattice expansion [22], but also a local deviation of the averaged composition was found, i.e. Fe is in an Fe-rich environment and Pt is in a Pt-rich environment. The usual Fourier transformation-based analysis of the EXAFS was complemented by a wavelet transformation method.

The composition inhomogeneities are likely the reason for the reduced magnetic moments of the nanoparticles by 20–30% with respect to the bulk material [12, 13] since the magnetic moments at the Fe sites are decreasing with increasing Fe content in the near environment. The latter dependence was found by SPR-KKR band structure calculations and XMCD experiments on bulk-like systems.

## Acknowledgments

We would like to thank S Sun (Brown U) for providing nanoparticles, J-U Thiele (Hitachi) for thin film preparation, and M Acet and T Krenke (U Duisburg-Essen) for the preparation of the bulk reference sample. We thank M Vennemann and M Acet (U Duisburg-Essen) for XRD measurements and for help in the XMCD

measurements, U Wiedwald (U Ulm), H-G Boyen (U Hasselt), N Friedenberger and S Stienen (U Duisburg-Essen) are acknowledged as well as P Voisin and S Feite (ESRF) for technical assistance, and the BESSY II staff, especially T Kachel and H Pfau, for their kind support. We thank M Košuth (LMU München), R Meyer and H Herper (U Duisburg-Essen) for helpful discussions.

This work was financially supported by the DFG (SFB445), the BMBF (05 ES3XBA/5), the ESRF and the EU (MRTN-CT-2004-0055667, 'SyntOrbMag').

## References

[1] Chantrell R W, Weller D, Klemmer T J, Sun S and Fullerton E E 2002 *J. Appl. Phys.* **91** 6866
[2] Antoniak C, Lindner J and Farle M 2005 *Europhys. Lett.* **70** 250
[3] Bian B, Laughlin D E, Sato K and Hirotsu Y 2000 *J. Appl. Phys.* **87** 6962
[4] Chen M-P, Nishio H, Kitamoto Y and Yamamoto H 2005 *J. Appl. Phys.* **97** 10J321
[5] Kim C K, Kan D, Veres T, Normadin F, Liao J K, Kim H H, Lee S-H, Zahn M and Muhammed M 2005 *J. Appl. Phys.* **97** 10Q918
[6] Ulmeanu M, Antoniak C, Wiedwald U, Farle M, Frait Z and Sun S 2004 *Phys. Rev.* B **69** 054417
[7] Dorman J L, Fiorani D and Tronc E 1997 *Adv. Chem. Phys.* **98** 283
[8] Ivanov O A, Solina L V, Demshina V A and Magat L M 1973 *Phys. Met. Metall.* **35** 81
[9] Visokay M R and Sinclair R 1995 *Appl. Phys. Lett.* **66** 1692
[10] Thiele J-U, Folks L, Toney M F and Weller D 1998 *J. Appl. Phys.* **84** 5686
[11] Shima T, Takanashi K, Takahashi Y K and Hono K 2004 *Appl. Phys. Lett.* **85** 2571
[12] Antoniak C *et al* 2006 *Phys. Rev. Lett.* **97** 117201
[13] Dmitrieva O *et al* 2007 *Phys. Rev.* B **76** 064414
[14] Newville M 2001 *J. Synchrotron Radiat.* **8** 322
[15] Mizuno M, Sasaki Y, Yu A C C and Inoue M 2004 *Langmuir* **20** 11305
[16] Yu A C C, Mizuno M, Sasaki Y, Inoue M, Kondo H, Ohta I, Djayaprawira D and Takahashi M 2003 *Appl. Phys. Lett.* **82** 4352
[17] Sun S, Anders S, Hamann H F, Thiele J-U, Baglin J E E, Thomson T, Fullerton E E, Murray C B and Terris B D 2002 *J. Am. Chem. Soc.* **124** 2884
[18] Stappert S, Rellinghaus B, Acet M and Wassermann E F 2003 *J. Cryst. Growth* **440** 252
[19] Dmitrieva O, Acet M, Dumpich G, Kästner J, Antoniak C, Farle M and Fauth K 2006 *J. Phys. D: Appl. Phys.* **39** 4741
[20] Li D, Poudyal N, Nandwana V, Jin Z, Elkins K and Liu J P 2006 *J. Appl. Phys.* **99** 08E911
[21] Wiedwald U, Klimmer A, Kern B, Han L, Boyen H-G, Ziemann P and Fauth K 2007 *Appl. Phys. Lett.* **90** 062508
[22] Antoniak C, Trunova A, Spasova M, Farle M, Wende H, Wilhelm F and Rogalev A 2008 *Phys. Rev.* B **78** 0401406R
[23] Sun S, Murray C B, Weller D, Folks L and Moser A 2000 *Science* **287** 1989
[24] Boyen H-G *et al* 2005 *Adv. Mater.* **17** 574
[25] Antoniak C and Farle M 2007 *Mod. Phys. Lett.* B **21** 1111
[26] Stöhr J, Sette F and Johnson A L 1984 *Phys. Rev. Lett.* **53** 1684
[27] Hitchcock A P, Beaulieu S, Stell T, Stöhr J and Sette F 1984 *J. Chem. Phys.* **80** 3927
[28] Ebert H *et al The Munich SPR-KKR Package, Version 3.6* http://olymp.cup.uni-muenchen.de/ak/ebert/SPRKKR
Ebert H 2000 Fully relativistic band structure calculations for magnetic solids—formalism and application *Electronic Structure and Physical Properties of Solids* (*Springer Lecture Notes in Physics* vol 535) ed H Dreyssé (Berlin: Springer) p 191
[29] Vosko S H, Wilk L and Nusair M 1980 *Can. J. Phys.* **58** 1200
[30] Pearson W B 1958 *A Handbook of Lattice Spacings and Structures of Metals and Alloys* (Oxford: Pergamon) p 634
[31] Grange W *et al* 1998 *Phys. Rev.* B **58** 6298
[32] Chen C T, Idzerda Y U, Lin H-J, Smith N V, Meigs G, Chaban E, Ho G H, Pellegrin E and Sette F 1995 *Phys. Rev. Lett.* **75** 152
[33] Thole B T, Carra P, Sette F and van der Laan G 1992 *Phys. Rev. Lett.* **68** 1943
[34] Carra P, Thole B T, Altarelli M and Wang X 1993 *Phys. Rev. Lett.* **70** 694
[35] Nakajima R, Stöhr J and Idzerda Y U 1999 *Phys. Rev.* B **59** 6421
[36] Fauth K 2004 *Appl. Phys. Lett.* **85** 3271
[37] Henke B L, Gullikson E M and Davis J C 1993 X-ray interactions: photoabsorption, scattering, transmission, and reflection at $E = 50$–$30\,000$ eV, $Z = 1$–$92$ *At. Data Nucl. Data Tables* **54** 181–342 http://henke.lbl.gov/optical_constants/
[38] Newville M, Livinš P, Yacoby Y, Rehr J J and Stern E A 1993 *Phys. Rev.* B **47** 14126
[39] Ravel B and Newville M 2005 *J. Synchrotron Radiat.* **12** 537
[40] Ankudinov A L, Ravel B, Rehr J J and Conradson S D 1998 *Phys. Rev.* B **58** 7565
[41] Zabinsky S I, Rehr J J, Ankudinov A, Albers R C and Eller M J 1995 *Phys. Rev.* B **52** 2995
[42] Newville M 2001 *J. Synchrotron Radiat.* **8** 96
[43] The FEFF project homepage http://leonardo.phys.washington.edu/feff/
[44] McKale A G, Veal B W, Paulikas A P, Chan S-K and Knapp G S 1998 *Phys. Rev.* B **38** 10919
[45] Faxén H and Holtsmark J 1927 *Z. Phys.* **45** 307
[46] Bunker G 1983 *Nucl. Instrum. Methods* **207** 437
[47] Kendall M G 1958 *The Advanced Theory of Statistics* vol 1 (London: Hodder Arnorld)
[48] Funke H, Scheinost A C and Chukalina M 2005 *Phys. Rev.* B **71** 094110
[49] Grossmann A and Morlet J 1984 *SIAM J. Math. Anal.* **15** 723
[50] Suzuki H, Kinjo T, Hayashi Y, Takemoto M and Ono K 1996 *J. Acoust. Emiss.* **14** 69
AGU-Vallen wavelet package http://www.vallen.de/wavelet/
[51] Wang R M, Dmitrieva O, Farle M, Dumpich G, Ye H Q, Poppa H, Kilaas R and Kisielowski C 2008 *Phys. Rev. Lett.* **100** 017205
[52] Perlov Ya, Ebert H, Yaresko A N, Antonov V N and Weller D 1998 *Solid State Commun.* **105** 273
[53] Galanakis I, Alouani M and Dreyssé H 2002 *J. Magn. Magn. Mater.* **242** 27
[54] Landolt H and Börnstein R 1986 *Numerical data and Functional Relationships in Science and Technology* (*New Series* vol III/19a) (Berlin: Springer) and references therein
[55] Herper H C, Hoffmann E and Entel P 1999 *Phys. Rev.* B **60** 3839
[56] Stöhr J and König H 1995 *Phys. Rev. Lett.* **75** 3748

[57] Ederer C, Komelj M and Fähnle M 2003 *Phys. Rev.* B **68** 052402

[58] Edmonds K W, Binns C, Baker S H, Thornton S C, Norris C, Goedkoop J B, Finazzi M and Brookes N B 1999 *Phys. Rev.* B **60** 472

[59] Labaye Y, Crisan O, Berger L, Greneche J M and Coey J M D 2002 *J. Appl. Phys.* **91** 8715

[60] Garanin D A and Kachkachi H 2003 *Phys. Rev. Lett.* **90** 065504